Available online at www.sciencedirect.com
SCIENCE DIRECT
Polymer 47 (2006) 3426–3435
polymer
www.elsevier.com/locate/polymer

Montmorillonite-thermoset nanocomposites via cryo-compounding

Hilmar Koerner [a], Devesh Misra [b], Ashley Tan [c], Lawrence Drummy [c], Peter Mirau [c], Richard Vaia [c,*]

[a] University of Dayton Research Institute, Dayton, OH, USA
[b] Department of Chemical Engineering, University of Louisiana at Lafayette, Lafayette, LA, USA
[c] Air Force Research Laboratory, Materials and Manufacturing Directorate, AFRL/MLBP, Bldg 654, 2941 Hobson Way, Wright-Patterson AFB, OH 45433-7750, USA

Received 23 December 2005; received in revised form 16 March 2006; accepted 17 March 2006

Abstract

For organically modified montmorillonite (OMM)–epoxy nanocomposites, maximal montmorillonite dispersion is found to depend synergistically on the mechanical processing history of the resin mixture and the chemistry at the OMM surface. Specifically, Cloisite 30A (quaternary ammonium OMM) and I30.E (primary ammonium OMM), each containing surfactants with different catalytic effects on the curing chemistry of Epon 862, are compared. Irrespective of the OMM, conventional solvent-free processing methodologies, including sonication, result in an inhomogeneous distribution of OMM on the micron scale. Even though the primary ammonium alkyls within I30.E enhance intragallery reactivity, this only results in extensive swelling of tactoids (interlayer distance ~10–20 nm), and thus retention of layer–layer correlations, leading to 'hybrid' micron scale reinforcing particles, not nanoscale dispersion of individual layers. In contrast, sub-ambient temperature (cryo) compounding had substantial impact on the ability to reduce tactoid and agglomerate size and increase homogeneity of dispersion for Cloisite 30A. The reactivity near Cloisite 30A is similar to that in the bulk and thus localized gelation around the layer-stacks does not retard particulate refinement. In all cases, alteration of the global epoxy network structure was ruled out by FTIR and NMR measurements. For nanocomposites with similar OMM content, however, the final thermal–mechanical properties does not coherently relate to one characteristic of the morphology. The coefficient of thermal expansion ($T > T_g$) and hardness ($T < T_g$) depend only weakly on morphology, where as the glass transition temperature depends strongly on the extent of OMM dispersion and interfacial chemistry. In general, the inter-relationships between mechanical processing, OMM surface chemistry and the desired property enhancements are not linear and thus must be considered in light of a final application to evaluate the optimal 'nanocomposite' fabrication methodology to achieve maximal benefit.

Keywords: Epoxy; Polymer nanocomposite; Layered silicate

1. Introduction

Nanoparticle additions to thermoset resins (thermoset nanocomposites) are being examined for a diverse range of applications, including in the aviation industry as epoxy adhesives and as matrices of structural fiber-reinforced composites [1–8]. This interest is due to the enhancement, or addition of, physical properties at low volume fractions of nanoparticles and the ability to incorporate the nanoparticles at various processing stages or at various locations within the engineered composite material (such as within the resin, between fiber plies and/or as a fiber sizing) based on the design requirements of the composite and the location within the composite that will yield maximal benefit.

In most cases, uniform dispersion [9] or controlled mesoscale association [10] of the nanoparticle is believed to be critical to maximize the property improvement. However, broad, quantitative verification of the relative importance of morphology and of interfacial strength for improvements of various physical properties (modulus, strength, permeability, conductivity, etc.) has not been ascertained [11–13]. Another major challenge is the development of new cost-effective methodologies to not only achieve uniform dispersion, but also achieve the desired interfacial characteristics between the nanoparticle and thermoset matrix. This is especially acute for nanoparticles that are initially a part of a low-dimensional crystallite [14], where the positions of individual 'nano'-layers or 'nano'-tubes within the crystallite (tactoid or rope, respectively) are related by translational symmetry. Extensive

* Corresponding author.: Tel.: +1 937 255 9184; fax: +1 937 255 9157.
E-mail address: richard.vaia@wpafb.af.mil (R. Vaia).

0032-3861/$ - see front matter © 2006 Elsevier Ltd. All rights reserved.
doi:10.1016/j.polymer.2006.03.057

mass transfer, at least to the extent of the largest dimension of the nanoparticle, is necessary to disrupt the initial correlations of these nano-layers or nano-tubes.

After tens of years of detailed research [15–18] the processing of thermoset layered silicate nanocomposites is still more an art than science. There are many contradicting and puzzling results concerning dispersion, intercalation or exfoliation [19]. Pioneering studies by Pinnavaia [1] on montmorillonite–epoxy systems established the initial conceptual methodology. Interfacial modifiers, such as primary ammonium alkyls, are intercalated between the montmorillonite layers to not only compatibilize the inorganic aluminosilicate and organic resin, but also to accelerate the cross-linking reaction between the layers through acid-catalysis. The enhanced so-called 'intragallery' versus 'extragallery' polymerization rate [19] results in increased monomer consumption within the swollen low-dimensional crystallite, and the continual increase of layer separation due to mass flow of monomer into the interlayers [20]. Unfortunately, homogenization of the dispersion necessitates Brownian motion of the individual layers, which is hindered by (i) interlayer orientational coupling arising from the original low-dimensional crystallite structure and (ii) extragallery polymerization which increases the medium's viscosity, ultimately leading to gelation. The result is an inhomogeneous dispersion on the micron scale of sub-micron 'hybrid' reinforcing fillers comprised of parallel layers separated by 5–20 nm of resin. Although these 'shadow tactoids' may be optimal for toughening [23], these morphologies are not optimal for stiffness as pointed out by Boyce et al. [11] who find that collections of layered silicates that are oriented parallel can be effectively represented as a homogeneous 'particle'. The parallel reinforcement ultimately leads to collective action and reduces the reinforcing effect per particle [11].

In general, sole reliance on Brownian motion and/or spatially inhomogeneous polymerization rates will not lead to uniform dispersion within the thermosets. The disturbance of the local orientational correlations between nanoparticles, and thus the 'shadow tactoids' must (1) occur in a pre-processing step well before the onset of gelation or (2) from high mechanical shear such as three-roll mill processing [21]. Recent reports on pre-processing innovations build off the initial methodology but address its limitations, such as slurry compounding [2,22,23] and surface initiated curing reaction in combination with slurry-processing [24]. These approaches lead to more homogenous dispersion paralleling that achievable in thermoplastics [25–27]. In contrast, the sole use of more mechanical shear appears fraught with difficulties due to the inherently low viscosity of the thermoset (relative to thermoplastic polymer melts) that leads to low mechanical coupling to the particle and thus a tendency to rotate and translate rather than rupture or break [28,29].

To further the understanding of epoxy–montmorillonite processing space and to provide alternative fabrication approaches enabling various degrees of interfacial coupling and morphologies for validation of structure–property relationships, we examine herein the impact of shear during the thermoset nanocomposite processing. We demonstrate that with the proper mechanical processing conditions, uniform dispersion and a high degree of exfoliation is possible in systems that typically only show intercalated morphologies after traditional cure cycles. Conceptually, this is achieved by maximizing thermoset viscosity by halting cure before gelation and by compounding at sub-ambient temperatures near the resin's glass transition temperature. High shear forces, due to the very high viscosity of the system, facilitate homogenization of the layered silicate nanocomposite in the thermoset. Since, this processing approach relies on interfacial compatibility and not necessarily on interfacial reactivity, the resulting nanocomposite possesses degrees of interfacial coupling and structure that are complementary to previous approaches. The weak interface of the nanocomposite fabricated herein leads to a substantial decrease in glass transition temperature.

2. Experimental

2.1. Materials

Organically modified montmorillonites (OMMs) used were Nanocor I.30E (145 mequiv/100 g, octadecylammonium bromide, $Mw_{surfactant} = 271$ g/mole, $\rho_{I30E} = 1.7$ g/cm^3, [30]) and Cloisite 30A (95 mequiv/100 g, methyl tallow bis-2-hydroylethyl ammonium, $Mw_{surfactant} \sim 361$ g/mole, $\rho_{30A} \sim 1.9$ g/cm^3, Southern Clay Products). OMMs underwent a cleaning routine consisting of soxhletting in ethanol, water and drying, yielding I.30E with 33.44 wt% organic (loss of ignition, LOI) and $d_{001} = 1.78$ nm; and SC30A with 33.42 wt% organic and $d_{001} = 1.85$ nm. The resulting material was ground into a fine powder with a ball mill and fractionated with a fine meshed copper sieve. Only the fraction with smallest particles was used in further experiments to obtain better dispersions and avoiding large agglomerates and crystallites. Note that the differences in number of surfactant molecules (CEC) and molecular weight per surfactant is approximately equivalent, and upon cleaning results in similar organic fraction (LOI) and initial gallery height (d_{001}). Thus, for an equivalent weight percentage of OMMs, nanocomposites possess the same volume fraction of layered silicate.

The thermoset matrix consisted of Epon 862 (bisphenol F epoxide) with diethyl-toluene diamine (Epikure W, Resolution Performance Products) with a ratio of 100:26 (density, $\rho_{matrix} \sim 1.03$ g/cm^3). The possible slight increase in amine concentration associated with the dissociation of a fraction of the alkyl primary ammonium surfactants on I30.E (see below) was not taken into account when balancing epoxide:amine stoichometry. Cure history was followed according to the product data sheet provided by Resolution Performance Products.

2.2. Characterization

OMM morphologies were determined via X-ray diffraction, transmission electron microscopy (TEM) and scanning electron microscopy (SEM). X-ray diffraction was conducted

on Bruker AXS D8 Discover and Molecular Metrology SAXS in transmission mode. Ultrathin sections for TEM were cut using a RMC PowerTome XL ultramicrotome equipped with a Diatome diamond knife. A cutting speed of 1 mm/s was used to cut 50 nm thick sections at room temperature. Sections were collected on 400 mesh copper grids. The sections were then coated with a thin layer ($\sim$10 nm) of amorphous carbon in order to improve the stability of the sections during electron irradiation. TEM was performed on a Philips CM 200 operating at 200 kV. A CCD camera was used for focusing at high magnification. Images were collected on SO-163 film and digitized using a Minolta DiMAGE scanner at 2400 dpi resolution. Image analysis was carried out by contrast thresholding the images and counting particles by incremental sections on 5×5 μm TEM image areas for two images each.

A first order estimate of the maximum number of montmorillonite layers per square micrometer ($N=n/A$), that could be viewed given complete single layer exfoliation can be derived from the definition of volume fraction of MMT (ϕ_{MMT} = total volume MMT/total volume of sample). Rearranging gives:

$$N = \frac{t}{V_{MMT}} \times \phi_{MMT}$$

where t is the thickness of the TEM thin section, n is the number of montmorillonite layers, A is the area of the thin section, and V_{MMT} is the average volume of a single montmorillonite sheet ($V_{MMT} \sim l^2 a$, where l is the layer diameter and a is the layer thickness). ϕ_{MMT} is related to volume fraction of OMM, ϕ_{OMM}, by the ratio of MMT layer thickness ($a \sim 1$ nm) to the interlayer repeat distance (d_{001}), $\phi_{MMT} = \phi_{OMM}\,(a/d_{001})$. ϕ_{OMM} is then related to the commonly used, weight fraction of OMM, χ_{OMM}, by: $\phi_{OMM} = \chi_{OMM}\rho_{OMM}^{-1}/\left(\chi_{OMM}\rho_{OMM}^{-1} + \left(1-\chi_{OMM}\right)\rho_{matrix}^{-1}\right)$. Note that the above expression inherently assumes that the thickness of the thin section, t, is equal to or greater than the largest dimension of the layer, l ($t \geq l$). For the systems examined herein, where $l \sim 80$ nm, $\rho_{OMM} \sim 1.8$ g/cm^3, $\rho_{matrix} \sim 1.0$ g/cm^3, $\chi = 0.03$, and $d_{001} \sim 1.8$ nm, $\phi_{OMM} = 0.0169$ and $\phi_{MMT} = 0.0094$. Using the limit of $t=1$ (note that 50 nm thin sections were utilized herein to maximize imaging conditions), $N \sim 117$ layers/μm^2 of TEM viewing area. For a random distribution of layers and recognizing that only layers with their surface normal in the plane of the thin section will have maximum contrast, $N_{observable} \sim 0.5$–0.67 N, conservatively [31]. Thus, for complete exfoliation of 3 wt% OMM, the number of observable montmorillonite sheets per square micrometers will be around 60.

Scanning electron microscopy (SEM) with energy dispersive spectroscopy (EDS) was carried out using a Thermo-Noran Vantage system on the Hitachi S-5200 microscope. Since, the electron beam generates the emission of X-rays characteristic of the elements present, this technique gives an elemental map of the surface.

IR spectra were obtained using a Thermo Nicolet Nexus 470 FT-IR with 32 scans at 16 cm^{-1} resolution on samples prepared with KBr pellets.

The solid-state carbon NMR spectra were acquired at 125 MHz on a Tecmag Apollo NMR spectrometer with a 5 mm magic-angle spinning probe from Doty Scientific, Inc. The spectra were acquired using cross polarization and 10 kHz magic-angle sample spinning using a 1 ms cross polarization time with 50 kHz fields applied to the proton and carbon channels. The pulse sequences for cross polarization and the T_1 and $T_{1\rho}$ relaxation times are described in the literature [32,33]. The 2D carbon-proton wideline (WISE) correlation experiment was used to indirectly measure the proton line widths through the more highly resolved carbon spectra [34]. The spectra were recorded with 64 points in the proton dimension using a sweep width of 300 kHz and time-proportional phase incrementation for quadrature detection in the proton dimension [35]. Two-phase pulse modulation was used for proton decoupling in all experiments [36].

Coefficient of thermal expansion at temperatures greater than the glass transition temperature ($T > T_g$) was obtained with a TA Instruments 2940 TM Analyzer at 4 °C/min. Reported values are the average of five samples with error bars representing standard deviations. Differential scanning calorimetry at 4 °C/min (TA Instruments Q1000) on 10 mg of sample verified complete cure for all OMM nanocomposites discussed, as well as providing the glass transition temperature of the system. DMA measurements were carried out using a TA Instruments DMA 2980 with a temperature ramp of 4 °C/min on $2\times1\times10$ mm^3 samples. Glass transition temperatures from DMA correspond to the temperature at the peak of tan δ.

Micro-indentation hardness tests (Vickers test) employed a weight onto the sample via a diamond shaped tip. Optical microscopy did not show micro cracks at the corners of the imprint implying reasonable toughness for all samples. From the diameter of the imprint and the force applied through the tip the hardness HV can be calculated according to $HV = 2F\sin(\theta/2)\times1000/d^2$ where F is the force in Newton, θ the angle of the shape of the tip (diamond = 45°) and d the length of the diagonal in μm that is measured from the imprint.

3. Results and discussion

3.1. Processing

Traditionally, organically modified montmorillonites (OMM) are combined with the epoxy resin, either neat [37] or with the help of a volatile solvent [38], followed by extensive mechanical mixing (sonication), the addition of the curing agent, potentially more mixing, degassing and finally curing. The application of mechanical mixing forces nominally occurs when the viscosity is relatively low, at least compared to that encountered in thermoplastic processing of nanocomposites. A low viscosity medium is ineffective in transferring shear stress to filler particles or polymer domains within an incompatible blend [39]. As the viscosity increases, however, the medium can more effectively transfer shear stress to a secondary phase, increasing the likelihood of refinement.

To increase viscosity for more effective mixing, a pre-cure (B-staging) to forward the cross-linking and increase molecular

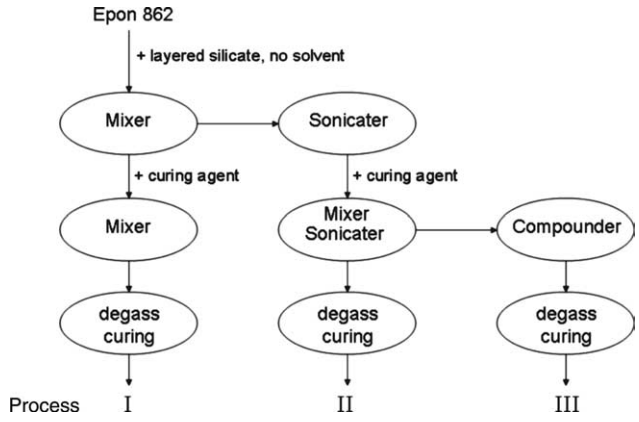

Fig. 1. Details of the methods (I, II, III) examined to determine the impact of variations in the use of mechanical mixing techniques on the OMM dispersion.

weight is an option, however, the increased molecular weight may comprise many subsequent processing properties and limit utility in VARTM and RTM (vacuum assisted resin transfer molding, resin transfer molding). Previous work by Benson-Tolle [40] has shown that B-staging provides a degree of control over layer–layer separation although these studies did not examine the impact of intermediate shearing steps or changes in global morphology. Alternatively, viscosity could be increased 'reversibly' by cooling the monomer mixture or progressed resin to near or below the glass-transition temperature and grinding/mixing, similar to the cryo-grinding (cryomilling or high-energy mechanical alloying) work of Torkelson et al. [41,42]. For thermoplastics, this has been shown to improve dispersion although concern about loss of aspect ratio has been noted [43,44].

Fig. 1 summarizes the three (I, II, III) processing methodologies discussed in this study. They represent the various stages and extent where mechanical mixing may be applied. The baseline epoxy cure procedure is based on Chen et al. [45]. Process I—mixing: OMM and epoxy were combined via simple dispersion and then underwent high-shear mixing (Ultra Turrax, IKA T18 basic, 18,000 rpm, 75C, 30 min). Adding Epikure W and further high-shear mixing with a final step of degassing and curing at 120 °C for 2 h; 175 °C for 2 h, lead to nanocomposite I. Process II—mixing and sonication: additional mixing of OMM and epoxy beyond process I included ultra-sonication (Ultrasonic Processor, Sonics and Materials, Inc., GEX600-5, 75C, 10 min) as well as additional high-shear mixing and ultra sonication after adding the curing agent (two cycles of 30 min mixing and 10 min sonication). Degassing and curing lead to nanocomposite II. Process III—compounding: for nanocomposite III, some material was separated from process II after the addition of the curing agent to undergo a compounding step at sub-ambient temperatures (DACA Instruments, CA, 250 RPM, torque 3–4 Nm). The samples were quenched with a water cooling bath and transferred to a DACA bench top twin-screw extruder were they were cycled for 30 min at −30 °C at a torque of 4 Nm and 250 rpm. The pasty suspension was then collected from the extruder and filled into a mold and degassed for the final curing reaction.

Temperatures at every mixing and sonication step (Ultra Turrax, Ultra Sonicator) were monitored using a temperature probe inside the nanocomposite suspension via a PID temperature controller and kept below 100 °C. Following this procedure, the progression of cure was kept as close as possible between the various systems. Typically, temperatures above 100 °C lead to uncontrollable cross-linking in all cases.

To further establish the role of the interfacial surfactant on the mechanical processing and cross-linking that may occur during mixing, primary ammonium modified montmorillonite (Nanocor I30.E, octadecylammonium bromide) and quaternary ammonium montmorillonite (Southern Clay Cloisite 30A, methyl tallow bis-2-hydroylethyl ammonium) were examined. The quaternary ammonium surfactant has been shown to enhance capability, especially when combined with solution-assisted processing, but otherwise has minimal catalytic activity (ROH, p$K_a \sim 16$, 25 °C [46]). In contrast, the slight acidity of the primary ammonium surfactants (RNH_3^+ pK_a 10.64, 25 °C) has been shown to catalyze epoxide condensation and first utilized by Pinnavaia [47] to enhance interlayer polymerization rates. Note that a primary ammonium itself will not react with an epoxide. Since, the extent of this catalysis, the potential incorporation of the liberated amine in the network and the maintenance of the ionic equilibrium at the aluminosilicate surface is unknown, a priori modification of the reaction stoichiometry to account for these effects is not possible.

Table 1 provides a summary of the morphologies resulting for the two OMMS and various processes. Figs. 2 and 3 summarize XRD and TEM characterization of primary and quaternary ammonium montmorillonites, respectively.

Table 1
Summary of local (X-ray) and global (TEM) morphology for process methods (I, II, III) (Fig. 1)

Sample/process	I	II	III
3 wt% I30.E Epon862/W d_{001} 3.75 nm			
Local (d_{001})	12.5 nm	12.5 nm	22 nm
Global	Poorly dispersed swollen tactoids	Poorly dispersed shadow tactoids, 2 particles/μm^2 [a]	Poorly dispersed shadow tactoids, little exfoliation, 8 particles/μm^2 [a]
3 wt% Cloisite 30A Epon862/W d_{001} 3.50 nm			
Local (d_{001})	3.39 nm	3.39 nm	3.30 nm
Global	Intercalated, poorly dispersed tactoids	Intercalated, poorly dispersed tactoids, 3 particles/μm^2 [a]	Exfoliated with well dispersed tactoids of 1–4 layers per tactoid, 37 particles/μm^2 [a]

[a] Average of two 50 μm^2 TEM micrographs. Ideally, single layer exfoliation would give ∼60 particles/μm^2 (Section 2).

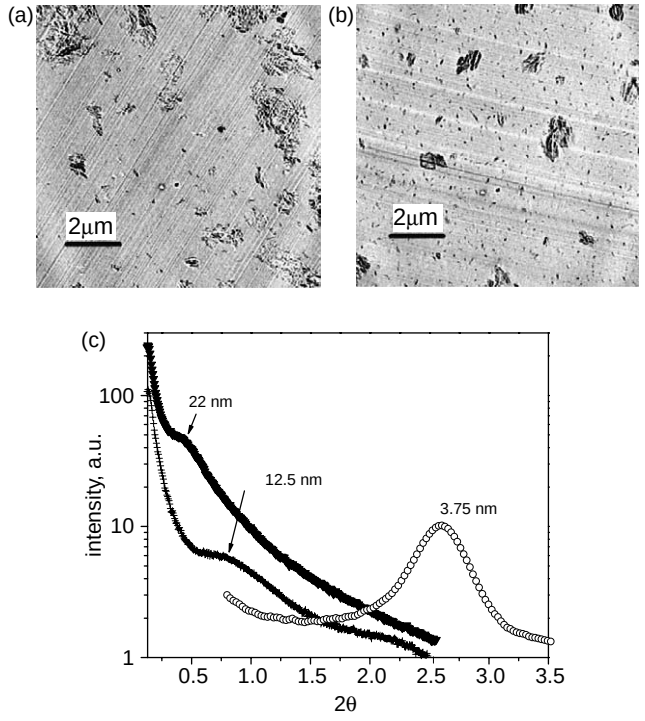

Fig. 2. Morphology of 3 wt% Nanocor I.30E in Epon 862/W. Transmission electron micrograph of (a) process II and (b) process III. (c) X-ray of (○) uncured resin with 3 wt% I.30E, (+) nanocomposite II (mixing, sonication) and (▼) nanocomposite III (compounding). Note that the curves are off-set vertically for clarity.

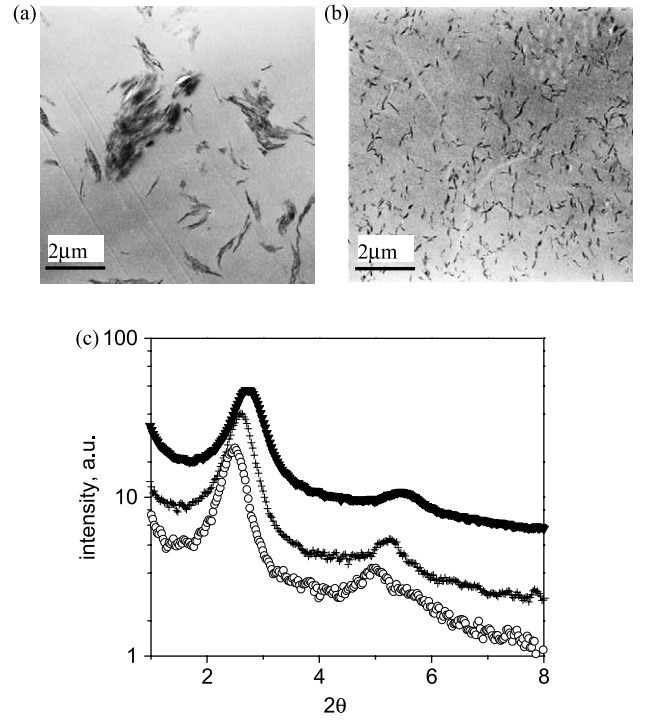

Fig. 3. Morphology of 3 wt% of Cloisite 30A in Epon 862/W. Transmission electron micrographs of (a) process II and (b) process III. (c) X-ray of (○) uncured resin with 3 wt% 30A, (+) nanocomposite II (mixing, sonication) and (▼) nanocomposite III (compounding). Note that the curves are off-set vertically for clarity.

For primary ammonium MMT (I30.E), Process I results in a swollen tactoid morphology with the OMM interlayer spacing increasing from 3.7 nm in the uncured state (Epon 862 and Epikure W) to 12.5 nm in the final nanocomposite (not shown). Further sonication (process II), does not result in further modification of the morphology (Fig. 2(a) and (c)). TEM images of these systems show poor dispersion and mostly swollen tactoids and agglomerates, with larger areas of neat epoxy resin. These observations are consistent with previous reports [45] and verify that there is a limit to the impact of shear processing on the local chemistries between the montmorillonite layers and on the extent that the particles can be broken down by mixing in the pre-cured resin (where the interlayer spacings are ~3–4 nm). In contrast, additional compounding (process III) when the resin viscosity is substantially larger leads to greater layer spacings, 22 nm (Fig. 2(b) and (c)). The amount of individual layers and the number of particles per square micrometers in the micrographs (Fig. 2(b)) are greater than that observed for process I and II. Nevertheless, despite the substantial increase in gallery spacing (Fig. 2(c)), the homogeneity of the dispersion is still poor and the morphologies are far from exfoliated.

The difficulty in achieving uniform dispersion for I30.E may possibly lie with the same process leading to gallery expansion—the enhanced polymerization rate catalyzed by acidic primary ammonium (or the Bronsted SiOH and AlOH acid groups on the MMT edges). In addition to layer swelling via mass transport, catalysis in the vicinity of the layered silicate, especially at the layer-edges, should also enhance cross-linking in the vicinity of the tactoids and thus locally decrease the time to gelation. This restricts the extent of layer separation in the vicinity of the tactoids and enhances the collective behavior of the layer-stacks in a shear field. Additionally, the larger the initial tactoid/agglomerate, the greater the absolute volume change of the tactoid/agglomerate necessary for uniform swelling. Swelling at the periphery of the tactoid/agglomerate will be facial compared to that at the center. This difference mediated by the stiffness of the aluminosilicate sheet will generate a heterogeneous stress distribution and retard the swelling rate of the inner most galleries. Thus, a collection of smaller agglomerates will be easier, and faster, to uniformly swell than one larger agglomerate containing all the layers. Mesoscopically, the smaller layer-stacks will increase the spatial uniformity of the catalysis at the onset of cure as well as providing for more facial swelling of the galleries at the center of the stack. With respect to this hypothesis, the larger layer spacing observed during Process III implies the compounding with elevated viscosities before complete curing enabled the tactoids to be broken into smaller primary particles, each containing fewer layers [48] and likely to swell further before gelation. This hypothesis then implies the final layer spacing in systems such as I30.E reflects a balance between local polymerization rate and tactoid size.

To qualitatively change the local polymerization, the same processing schemes were applied to an alkyl quaternary ammonium montmorillonite (Cloisite 30A), which lacks

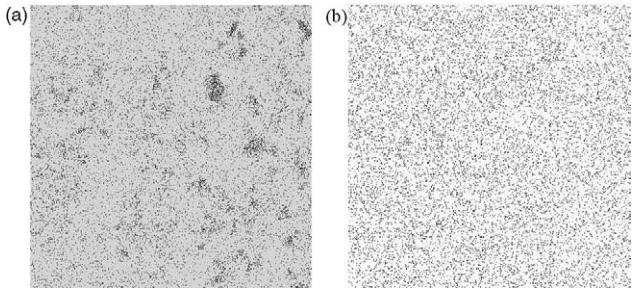

Fig. 4. Energy dispersive spectroscopy image (1600 μm^2 area, scanning electron microscope) of (a) sonicated (II) Cloisite 30A nanocomposite and (b) compounded (III) Cloisite 30A nanocomposite, comparing the uniformity of inorganic dispersion.

the acidic proton arising from equilibrium between the primary ammonium and amine. Here, the layer spacing does not increase with cure and is approximately the same for the initial uncured mixture and all process histories (Fig. 3, Table 1). This contrast with the I30.E nanocomposites is consistent with the supposition that layer spacing within a final, cured nanocomposite is primarily determined by interlayer reactivity. The TEM, Fig. 3(a), of the mixed and mixed/sonicated samples (process I and process II, respectively) shows similar global morphology as I30.E, however, with no swelling of tactoids. In apparent contradiction with the X-ray results, however, the TEM image of the compounded nanocomposite (process III, Fig. 3(b)) shows extremely uniform dispersion of particles; approximately 37 particles per square micrometers, consisting of particles containing 2–4 layers along with a large portion of single layers. These image statistics are approaching estimated values for complete layer exfoliation ($\sim$60 layers/μm^2). The distinct d_{001} reflection (Fig. 3(c)) with an unchanged correlation length (full width at half maximum) indicates that the tactoids with 2–4 layers have retained the original internal structure. These XRD results are consistent with previous modeling studies on the impact of disorder and layer-stack size on the d_{001} reflection, where only 3–5 layers are necessary to provide good correlation and intense diffraction peaks [14].

To further verify large scale homogeneity of the compounded Cloisite 30A nanocomposite, Fig. 4 compares electron dispersive spectroscopy maps of elemental Si distribution of the compounded (III) and sonicated (II) Cloisite 30A nanocomposites. Even at this low magnification (a 40×40 μm^2 window is shown), Si distribution is uniform for process III (Fig. 4(b)), whereas significant inhomogeneities of Si concentration are seen for process II (dark areas in Fig. 4(a)).

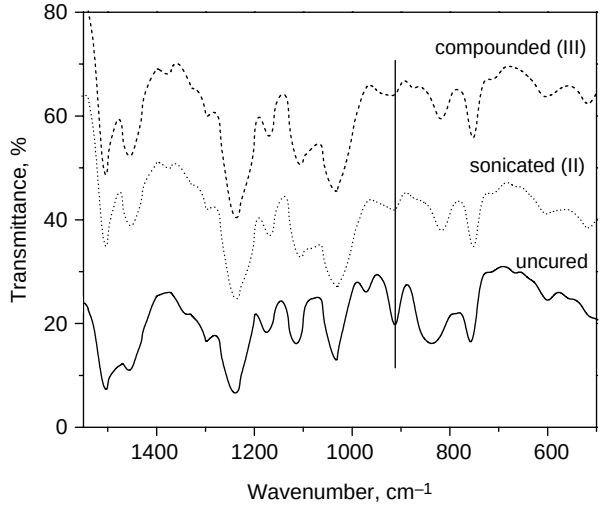

Fig. 5. FTIR of 3 wt% Cloisite 30A in Epon 862/W ((—) uncured formulation, (···) sonicated (II) nanocomposite, and (– –) compounded (III) nanocomposite) showing no dependency of matrix chemistry on varying processing history. Vertical line denotes the antisymmetric in-phase epoxide ring stretching at 910 cm^{-1}.

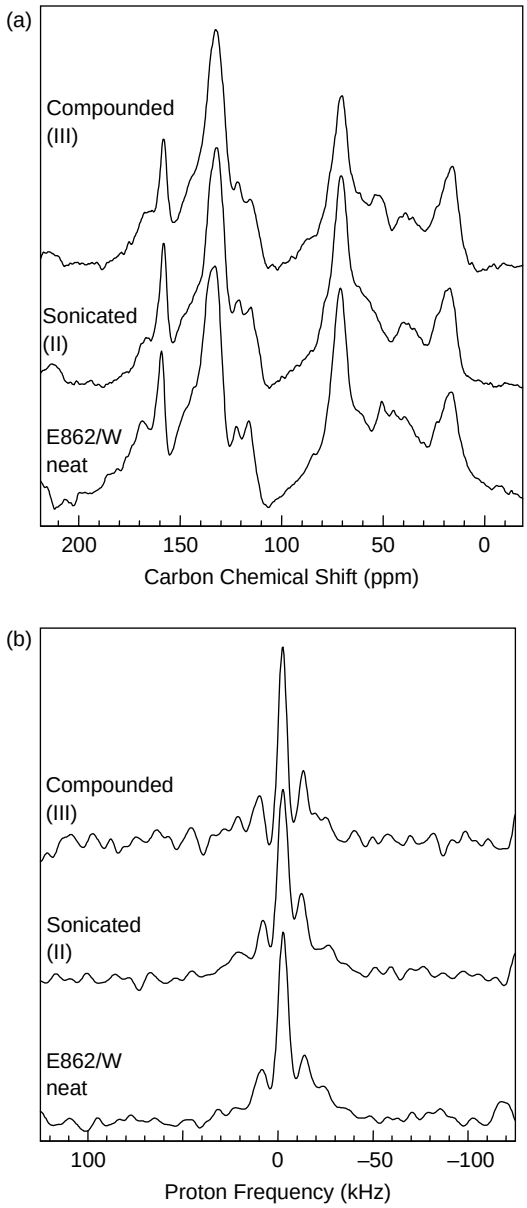

Fig. 6. (a) NMR spectra: (bottom) cured neat Epon862/W; (middle) sonicated (II) 3 wt% Cloisite 30A nanocomposite and (top) compounded (III) 3 wt% Cloisite 30A nanocomposite. (b) WISE spectra for the aromatic carbons: (bottom) cured neat Epon862/W; (middle) sonicated (II) 3 wt% Cloisite 30A nanocomposite; and (top) compounded (III) 3 wt% Cloisite 30A nanocomposite.

Overall, the contrast between the primary and quaternary OMMs indicates that for homogeneous morphologies initial tactoid size is at least as important, if not more so, than intra-gallery polymerization rate. To further support this conclusion the minimal impact of compounding on the development of the epoxy network needs to be verified.

Differential scanning calorimetry (TA Instruments Q1000) verified complete cure for all processes, cure histories and concentrations of OMM examined (Table 1). Further verification that the final epoxy matrix is similar and independent of mixing history was provided by FTIR and NMR. Focusing on Cloisite 30A (results are similar for I30E), the decrease of the epoxy band at 910 cm^{-1} (Fig. 5) is the same for both the compounded (III) and sonicated (II) sample, and not affected by the presence of nanofillers.

Fig. 6(a) shows the 125 MHz solid state carbon spectra for Epon 862 and the composites with Cloisite 30A prepared by II and III. The broad lines in Fig. 6(a) are a consequence of the many non-equivalent carbon atoms in such a network structure. Among the peaks of interest are the aromatic carbons bonded to oxygen atoms near 160 ppm, the aromatic carbons between 150 and 110 ppm, the methylene carbons bonded to oxygens near 70 ppm and other aliphatic carbons between 50 and 20 ppm. While the individual peaks are not well resolved, we would expect that the peak intensities and line shapes would be sensitive to gross changes in the network structure. With in the signal-to-noise limits of this experiment, we do not detect any large differences in the network structure by NMR.

NMR relaxation methods were used to evaluate the structure and dynamics of the resins and composites at room temperature [32,33]. The carbon and proton spin–lattice (T_1) and the proton rotating-frame relaxation times ($T_{1\rho}$) are listed in Table 2. The proton T_1s are sensitive to megahertz frequency molecular motions and the presence of any paramagnetic ions contained in the Cloisite 30A samples. Magnetization is rapidly exchanged between nearby protons in solids (a process known as spin diffusion), leading to averaging of the proton relaxation times. It has been previously noted that the paramagnetic contribution to the proton relaxation time is sensitive to the dispersion of the clay platelets [49–51]. The data in Table 2 show that the proton T_1s for the sonicated (II) and compounded (III) samples are similar to each other, but shorter than the values observed for neat Epon 862. The proton $T_{1\rho}$ relaxation times, which are sensitive to molecular motions on the kilohertz time scale, show a similar pattern. The carbon relaxation times are not averaged by proton spin diffusion and are more sensitive to the molecular dynamics. The relaxation times for the aromatic carbons are quite long (as expected for aromatic carbons below the glass transition temperature) and not very sensitive to the presence of the clay. Taken together the relaxation data do not show a large difference in the structure or dynamics between the sonicated (II) and compounded (III) samples.

Table 2
Relaxation times from cross polarization and magic-angle spinning

Sample	^{1}H T_1 (s)	^{1}H $T_{1\rho}$ (ms)	^{13}C T_1 (s)
Epon862	3.7	4.4	19
3 wt% Epon862/30A sonicated (II)	2.2	3.6	–
3 wt% Epon862/30A compounded (III)	2.0	3.6	24

The proton spectra of polymers are often broad and featureless because of the dipolar interactions between nearby spins. The line widths for polymers below T_g are typically on the order of 50–60 kHz, but the line widths can be greatly reduced by large amplitude molecular motions. We have measured the proton line widths indirectly using 2D wide line correlation NMR [34], and the proton line shapes for neat Epon 862 and the sonicated and compounded Cloisite 30A samples are shown in Fig. 6(b). Without a detailed analysis it can be seen that similar line shapes are observed for all three samples. This shows that there is not a large difference in the kilohertz frequency dynamics for the aromatic rings in the neat Epon 862 and the sonicated and compounded Cloisite 30A nanocomposites.

Thus, within the resolution of general spectroscopic techniques, the epoxy network structure, the extent of cure and global dynamics are independent of process history.

3.2. Physical properties

Although the volume fraction of montmorillonite is similar, the physical characteristics of these epoxy nanocomposites are anticipated to be divergent given the various morphologies and different interfacial surfactants. However, this is not the case in general.

Fig. 7 compares hardness from micro-indentation tests at room temperature (Vickers test) and coefficient of thermal expansion (CTE) above the glass transition temperature for the various layered silicate nanocomposites. No differences in hardness with respect to the addition of montmorillonite, or the various morphologies (compounded (III) and sonicated (II) samples), is observed. For CTE, although the absolute value decreases with addition of montmorillonite, the CTE only marginally depends on morphology. The slightly higher values of CTE observed for I30.E compared to Cloisite 30A nanocomposites may reflect a slight stoichiometic off-set arising from the reactivity of the I30.E surfactants (see below).

Fig. 8 summarizes the dynamic mechanical analysis of

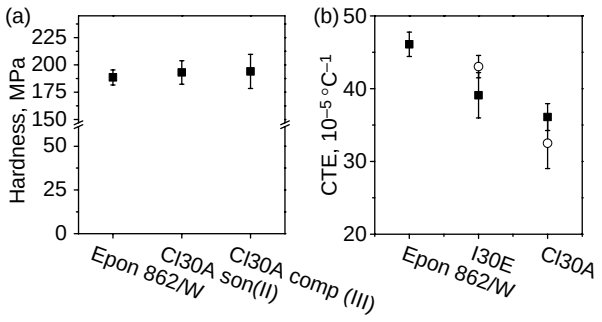

Fig. 7. (a) Vickers hardness for neat Epon 862/W and 3 wt% Cloisite 30A nanocomposites. (b) Coefficient of thermal expansion (CTE) at $T > T_g$ for neat epoxy and various processing of 3 wt% Cloisite 30A and 3 wt% Nanocor I.30E nanocomposites: (■) sonicated (II); (○) compounded (III).

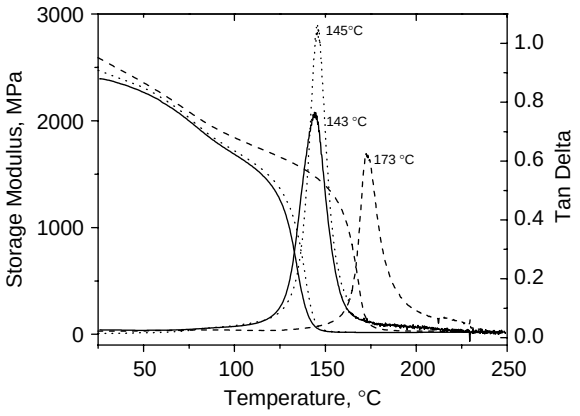

Fig. 8. Storage modulus and tan δ from dynamic mechanical analysis for 3 wt% Cloisite 30A sonicated (II) (– –), compounded (III) (·) and neat Epon 862 compounded (III) (—).

Cloisite 30A nanocomposites. Complementing the Vicker's test results, little difference beyond experimental uncertainty is observed in the storage modulus at room temperature (~2.5 GPa) between the morphologies (process II and III samples) and unfilled epoxy processed similarly (III). Furthermore, the room temperature moduli between Cloisite 30A and I30.E nanocomposites, either compounded (III) or sonicated (II), were comparable (not shown).

Differences, however, arise in the region surrounding the glass transition temperature (T_g), implying the different dispersions and interfaces have an impact on the cooperative network relaxation. Table 3 summarizes the T_gs determined by DMA and DSC. The T_gs determined by DSC were consistently 17–19 °C lower than determined by DMA and exhibited the same trends.

Although the compounded Cloisite 30A nanocomposite has a more uniform morphology, the T_g from DMA (145 °C) is close to that of the pure epoxy (143 °C), and substantially lower than that of the sonicated 30A sample (172 °C), which exhibits a less uniform morphology. The width and shape of the alpha transition of Cloisite 30A nanocomposites and the neat epoxy are similar (Fig. 8), indicating that the distribution in relaxation times (and the associated distribution in local environments) within the epoxy are similar—just that the mean relaxation time of the network has changed. Overall, the decrease in T_g with increased montmorillonite dispersion can be taken as a direct reflection of interfacial plasticization and/or disruption of the thermoset network arising from the greater interfacial area of a non-reactive surface in the compounded (III) 30A. Increased number density of non-reactive nano-scale layers, which can yield 700–800 $\mu m^2$of interfacial area per cubic micrometers of layers [52], will effectively slice through the network structure, disrupting a plane of cross-links every 15–20 nm at only 5–7 vol% OMM addition [53]. As interfacial area increases with dispersion, both plasticization and disruption of the network topology would become more pronounced. At temperatures greater than T_g though, the extent of reinforcement, rather than interfacial details, appears to dominate the impact of the OMM addition, as indicated by the similar CTEs. The slightly lower CTE value from the compounded (III) Cloisite 30A may simply reflect the more uniform dispersion of a filler with a substantially lower bulk expansivity than that of the medium. The more uniform distribution and smaller mean particle–particle distances would better constrain expansion of the majority of the molten epoxy network.

In contrast to 30A, the I30.E nanocomposites exhibited a much smaller impact on T_g ($\Delta T_g \sim 5$ °C, Table 3) due to processing differences. This is not completely unexpected given that there were only moderate changes in morphology. The addition of 3 wt% I30E, though, increased T_g relative to the unfilled epoxy (15–20 °C) less than that observed for the sonicated (II) 30A, which exhibited qualitatively similar global morphology. The reduced effectiveness of I30.E relative to 30A, whether in increasing T_g or reducing the CTE at $T > T_g$, may be related to the different molecular details at the montmorillonite–epoxy interface. Recall that the extent of cure and the chemistry of the epoxy network are, within the experimental resolution of DSC, FTIR and NMR, identical for the different processing techniques and OMMs. Nevertheless, the relatively diminished 'reinforcement' effect of a moderate dispersion of I30E (process II) (Table 1, Table 3, Fig. 7) could reflect an increase in epoxide condensation and concomitant offset of stoichiometry that is below the resolution limit of the aforementioned spectroscopic techniques; thus modifying network topology and reducing the effective T_g. Note that both OMMs have the same organic content, so extent of plasticization associated with the surfactants would be comparable for comparable morphologies. Overall, however, attributing these differences in CTE and T_g to plasticization or changes in network architecture is far from straightforward due to numerous counteracting factors. The molecular details of the MMT–epoxy interface and impact on macroscopic properties may depend on the surfactant content, the interfacial area (depends on extent of dispersion), the extent of alkyl primary ammonium incorporation in the epoxy network, the concomitant decrease in CEC of the MMT, and the degree of solubilization of the alkyl quaternary ammonium by the epoxy network. Quantitatively detailing mesoscopic 3D connectivity and the impact of the OMM on the topology and dynamics of the networks near the montmorillonite surface is at this time beyond currently standard analytical techniques.

Table 3
Glass transitions obtained from DSC and DMA data

Sample	Epon862/I30.E (3 wt%)		Epon862/30A (3 wt%)		Neat Epon 862	
	Sonicated (II)	Compounded (III)	Sonicated (II)	Compounded (III)	Sonicated (II)	Compounded (III)
T_g (°C) DSC	144	140	153	126	136	131
T_g (°C) DMA	163	157	172	145	–	144

4. Conclusion

The comparison of global morphology and the thermal–mechanical properties of montmorillonite–epoxy nanocomposites with respect to process history and interfacial chemistry provides conceptual insight to clarify the complex inter-relationships between processing, morphology and properties, as well as validating a technologically-relevant methodology to maximize dispersion in these systems through mechanical means.

Cloisite 30A (Southern Clay), a quaternary OMM, and I30.E (Nanocor), a primary OMM, contain surfactants with different catalytic effects on the curing chemistry of the Epon 862 epoxy matrix. Irrespective of the OMM, conventional processing results in poor global dispersion, large agglomerates, tactoids and large areas of neat epoxy. Sub-ambient temperature (cryo) compounding has only little impact on breaking these tactoids/agglomerates apart for I30.E, probably reflecting the enhanced cross-link density around the swollen OMM layers due to the enhanced catalysis of the curing reaction within the interlayer and at the layer edges. In contrast, sub-ambient temperature (cryo) compounding had substantial impact on the ability to reduce tactoid and agglomerate size and increase homogeneity of dispersion for Cloisite 30A. The reactivity near Cloisite 30A is similar to that in the bulk and thus localized gelation around the layer-stacks does not retard particulate refinement. In these cases, alteration of the global epoxy network structure was ruled out by FTIR and NMR measurements. Additionally, complete morphology validation could only be accomplished with a systematic combination of electron microscopy (TEM, SEM EDS) and small angle X-ray scattering. The global-scale morphology was not consistent with simple interpretation of the position and strength of X-ray scattering peaks.

Thus, according to these findings, minimizing initial tactoid size before the onset of gelation is critical in obtaining uniform dispersion and exfoliation. Traditional concepts of enhancing intra-gallery polymerization rates restrict the ability to decrease the tactoid size (as defined by the number of orientationally coherent layers).

Despite the substantial differences in the morphology of the cryo-compounded nanocomposites, their thermal–mechanical properties (DMA and TMA) were very similar. However, the increased uniformity of the Cloisite 30A did not increase the glass transition temperature in comparison to I30.E or traditionally-processed Cloisite 30A nanocomposites. Competing effects associated with increased OMM dispersion—rigid-phase reinforcement versus disruption of the extent of epoxy network topology and plasticization by non-reactive surfactants—probably negate one another resulting in a glass transition comparable to the unfilled epoxy.

On the whole, the cryo-compounding of thermoset nanocomposites provides a unique alternative to current thermoset nanocomposite fabrication methods. However, it must be noted that many applications of thermosets have viscosity limitations (such as RTM or VATRM). The cryo-compounding fundamentally relies on high matrix viscosity to enhanced refinement of the filler, and thus is limited in its applicability to these low-cost composite fabrication techniques. Nevertheless, adhesive technologies and pre-preg formation are felt to be amenable to these concepts.

Finally, this study shows that it is crucial to balance the OMM interfacial chemistry (surfactants) and the processing history for successful dispersion and exfoliation of OMM in thermosets. However, optimizing dispersion and exfoliation may not lead to the desired or anticipated improvements in mechanical and thermal properties, especially when the interface between resin and OMM is ‘soft’ and not ideal (perfect bonding). In general, the inter-relationships between OMM surface chemistry, mechanical processing and the desired property enhancements are not linear and thus must be considered in light of a final application to evaluate the optimal ‘nanocomposite’ fabrication methodology to achieve maximal benefit.

Acknowledgements

We would like to thank G. Price, M. Houtz (UDRI) for help with X-ray and TMA experiments, Dave Tomlin for SEM, Karen Farmer for assistance in microtoming. L.D. is supported through the National Research Council Fellowship Program. The Air Force Office of Scientific Research; the Air Force Research Laboratory and the Materials and Manufacturing Directorate provided funding.

References

[1] Lan T, Kaviratna PD, Pinnavaia TJ. Synthesis, characterization and mechanical properties of epoxy–clay nanocomposites. Polym Mater Sci Eng 1994;71:527.
[2] Brown JM, Curliss D, Vaia RA. Thermoset-layered silicate nanocomposites. Quaternary ammonium montmorillonite with primary diamine cured epoxies. Chem Mater 2000;12(11):3376–84.
[3] Singh B, Jagtap RN. Polymer clay nanocomposites: a review. Popular Plast Packaging 2002;47(3):51–9 (see also p. 64).
[4] Kornmann X, Lindberg H, Berglund LA. Synthesis of epoxy–clay nanocomposites. Influence of the nature of the curing agent on structure. Polymer 2001;42:4493–9.
[5] Ganguli S, Dean D, Jordon K, Price G, Vaia R. Mechanical properties of intercalated cyanate ester-layered silicate nanocomposites. Polymer 2003; 44:1315–9.
[6] Zilg C, Mülhaupt R, Finter J. Morphology and toughness/stiffness balance of nanocomposites based upon anhydride-cured epoxy resins and layered silicates. Macromol Chem Phys 1999;200(3):661–70.
[7] Zerda AS, Lesser AJ. Intercalated clay nanocomposites: morphology, mechanics, and fracture behavior. J Polym Sci, Part B: Polym Phys 2001; 39(11):1137–46.
[8] Becker O, Cheng Y-B, Varley RJ, Simon GP. Layered silicate nanocomposites based on various high-functionality epoxy resins: the influence of cure temperature on morphology, mechanical properties, and free volume. Macromolecules 2003;36(5):1616–25.
[9] Park S-J, Seo D-I, Lee J-R, Kim D-S. Synthesis and characterization of epoxy/clay nanocomposites. Kongop Hwahak 2001;12(2):181–5.
[10] Fornes TD, Paul DR. Modeling properties of nylon 6/clay nanocomposites using composite theories. Polymer 2003;44:4993–5013.
[11] Sheng N, Boyce MC, Parks DM, Rutledge GC, Abes JI, Cohen RE. Multiscale micromechanical modeling of polymer/clay nanocomposites and effective clay particle. Polymer 2004;45:487–506.
[12] Gusev AA, Lusti HR. Rational design of nanocomposites for barrier applications. Adv Mater 2001;13(21):1641–3.

[13] Gusev AA, Rozman MG. Numerical search for morphologies providing ultra high elastic stiffness in filled rubbers. Comput Theor Polym Sci 1999;9:335–7.
[14] Vaia R, Liu W, Koerner H. Analysis of small-angle scattering of suspensions of organically modified montmorillonite: implications to phase behavior of polymer nanocomposites. J Polym Sci, Part B: Polym Phys 2003;41:3214–36.
[15] Okada A, Kawasumi M, Usuki A, Kojima T, Kamigaito O. Polymer based molecular composites. In: Schaefer DW, Mark JE, editors. MRS symposium proceedings, Pittsburgh, vol. 171; 1990. p. 45–50.
[16] Alexandre M, Dubois P. Polymer-layered silicate nanocomposites: preparation, properties and uses of a new class of materials. Mater Sci Eng 2000;28:1–63.
[17] Pinnavaia TJ, Beall GW, editors. Polymer–clay nanocomposites. Wiley series in polymer science. New York: Wiley; 2000.
[18] Ray SS, Okamoto M. Polymer/layered silicate nanocomposites: a review from preparation to processing. Prog Polym Sci 2003;28:1539–641.
[19] Triantafillidis CS, LeBaron PC, Pinnavaia TJ. Thermoset epoxy–clay nanocomposites: the dual role of a,w-diamines as clay surface modifiers and polymer curing agents. J Solid State Chem 2002;167:354–62.
[20] Vaia RA, Liu W. X-ray powder diffraction of polymer/layered silicate nanocomposites: model and practice. J Polym Sci, Part B: Polym Phys 2002;40(15):1590–600.
[21] Yasmin A, Abot JL, Daniel IM. Processing of clay/epoxy nanocomposites by shear mixing. Scripta Mater 2003;49:81–6.
[22] Chen B, Liu J, Chen H, Wu J. Synthesis of disordered and highly exfoliated epoxy/clay nanocomposites using organoclay with catalytic function via acetone–clay slurry method. Chem Mater 2004;16:4864–6.
[23] Wang K, Chen L, Wu J, Toh ML, He C, Yee AF. Epoxy nanocomposites with highly exfoliated clay: mechanical properties and fracture mechanisms. Macromolecules 2005;38:788–800.
[24] Ma J, Yu ZZ, Zhang QX, Xie XL, Mai YW, Luck I. A novel method for preparation of disorderly exfoliated epoxy/clay nanocomposite. Chem Mater 2004;16(5):757–9.
[25] Fornes TD, Yoon PJ, Hunter DL, Keskkula H, Paul DR. Effect of organoclay structure on nylon 6 nanocomposite morphology and properties. Polymer 2002;43(22):5915–33.
[26] Manias E, Touny A, Wu L, Strawhecker K, Lu B, Chung TC. Polypropylene/montmorillonite nanocomposites. Review of the synthetic routes and materials properties. Chem Mater 2001;13:3516–23.
[27] Wang ZM, Nakajima H, Manias E, Chung TC. Exfoliated PP/clay nanocomposites using ammonium-terminated PP as the organic modification for montmorillonite. Macromolecules 2003;36(24):8919–22 [Communication].
[28] Cassagnau P, Michel A. New morphologies in immiscible polymer blends generated by a dynamic quenching process. Polymer 2001;42(7): 3139–52.
[29] Ziegler VE, Wolf BA. On the role of drop break up for coalescence processes and morphology development in polymer blends under shear. Macromolecules 2005;38(13):5826–33.
[30] G-105 Polymer grade montmorillonite, Product Sheet (3-29-04), Nanocor, Inc., Arlington Heights, IL.
[31] Drummy LF, Koerner H, Farmer K, Tan A, Farmer BL, Vaia RA. High-resolution electron microscopy of montmorillonite and montmorillonite/epoxy nanocomposites. Chem Phys B 2005;109(38):17868–78.
[32] Komoroski RA. High resolution NMR spectroscopy of synthetic polymers in bulk, vol. 7. Dearfield Beach: VCH Publishers Inc. 1986.
[33] Mirau P. In: A practical guide to the NMR of Polymers. Hoboken: Wiley; 2004. p. 418.
[34] Schmidt-Rohr KJ, Clauss H, Spiess H. Correlation of structure, mobility, and morphological information in heterogeneous polymer materials by two-dimensional wideline separation NMR spectroscopy. Macromolecules 1992;25:3273–7.
[35] Marion DK, Wuthrich K. Biochem Biophys Res Comm 1983;113:967.
[36] Bennett AE, Rienstra OM, Auger M, Lakshmi KV, Griffin RG. Heteronuclear decoupling in rotating solids. J Chem Phys 1995;103: 6951–8.
[37] Brown JM, Curliss D, Vaia RA. Thermoset-layered silicate nanocomposites. Quaternary ammonium montmorillonite with primary diamine cured epoxies. Chem Mater 2000;12(11):3376–84.
[38] Chen B, Liu J, Chen H, Wu J. Synthesis of disordered and highly exfoliated epoxy/clay nanocomposites using organoclay with catalytic function via acetone-clay slurry method. Chem Mater 2004;16:4864–6.
[39] Tucker CLI, Moldenaers P. Microstructural evolution in polymer blends. Annu Rev Fluid Mech 2002;34:177–210.
[40] Chen C, Tolle TB. Fully exfoliated layered silicate epoxy nanocomposites. J Polym Sci, Part B: Polym Phys 2004;42:3981–6.
[41] Furgiuele N, Lebovitz AH, Khait K, Torkelson JM. Novel strategy for polymer blend compatibilization: solid-state shear pulverization. Macromolecules 2000;33:225.
[42] Lebovitz AH, Khait K, Torkelson JM. Sub-micron dispersed-phase particle size in polymer blends: overcoming the Taylor limit via solid-state shear pulverization. Polymer 2003;44(1):199–206.
[43] Zhu YG, Li ZQ, Zhang D, Tanimoto T. Abs/iron nanocomposites prepared by cryomilling. J Appl Polym Sci 2005;99:501–5.
[44] Andrews T, Jacque D, Qian D, Rantell T. Multiwall carbon nanotubes: synthesis and application. Acc Chem Res 2002;35:1008–17.
[45] Chen C, Curliss D. Processing and morphological development of montmorillonite epoxy nanocomposites. Nanotechnology 2003;14: 643–8.
[46] Brown HC, et al. In: Braude EA, Nachod FC, editors. Determination of organic structures by physical methods. New York: Academic Press; 1995.
[47] Shi H, Lan T, Pinnavaia TJ. Interfacial effects on the reinforcement properties of polymer–organoclay nanocomposites. Chem Mater 1996;8: 1584–7.
[48] Janssen JMH, Meijer HEH. J Rheol 1993;37(4):597–608.
[49] VanderHart DL, Asano A, Gilman JW. NMR measurements related to clay-dispersion quality and organic-modifier stability in nylon-6/clay nanocomposites. Macromolecules 2001;34:3819.
[50] Levin EM, Hou SS, Bud'ko SL, Schmidt-Rohr K. J Appl Phys 2004;96: 5085.
[51] Koerner H, Hampton E, Dean D, Turgut Z, Drummy L, Mirau P, et al. Generating tri-axial reinforced epoxy montmorillonite nanocomposites with uni-axial magnetic fields. Chem Mater 2005;18:1990–6.
[52] Vaia RA, Wagner HD. Framework for nanocomposites. Mater Today 2004;7(11):32–7.
[53] Vaia RA, Giannelis EP. Polymer Nanocomposites: status and opportunities. MRS Bull 2001;36:394.